Submitted to ApJ April 24, 2017
Preprint typeset using LaTeX style emulateapj v. 01/23/15

COMMUNITY TARGETS FOR JWST'S EARLY RELEASE SCIENCE PROGRAM: EVALUATION OF WASP-63b

Brian M. Kilpatrick[1], Patricio E. Cubillos,[2], Kevin B. Stevenson[3], Nikole K. Lewis[3], Hannah Wakeford[4], Ryan J. MacDonald[5], Nikku Madhusudhan[5], Jasmina Blecic[6], Giovanni Bruno [3], Adam Burrows[7], Drake Deming[8], Kevin Heng[9], Michael R. Line[10], Caroline V. Morley[11],[18], Vivien Parmentier[12],[18], Gregory S. Tucker[1], Jeff A. Valenti[3], Ingo P. Waldmann[13], Jacob L. Bean[14], Charles Beichman[15], Jonathan Fraine[3], J. E. Krick[16], Joshua D. Lothringer[12], Avi M. Mandell[17]

1. Department of Physics, Box 1843, Brown University, Providence, RI 02904, USA
2. Space Research Institute, Austrian Academy of Sciences, Schmiedlstrasse 6, A-8042 Graz, Austria
3. Space Telescope Science Institute, Baltimore, MD 21218, USA
4. Planetary Systems Lab, NASA Goddard Space Flight Center, Greenbelt, MD 20771, USA
5. Institute of Astronomy, University of Cambridge, Madingley Road, Cambridge, CB3 0HA, UK
6. Department of Physics, New York University Abu Dhabi, P.O. Box 129188 Abu Dhabi, UAE
7. Department of Astronomy, University of Maryland, College Park, MD 20742, USA; ddeming@astro.umd.edu
8. Department of Astronomy, University of Maryland, College Park, MD 20742, USA
9. University of Bern, Center for Space and Habitability, Sidlerstrasse 5, CH-3012, Bern, Switzerland
10. School of Earth & Space Exploration, Arizona State University, Phoenix, AZ 85282, USA
11. Department of Astronomy, Harvard University, Cambridge, MA 02138, USA
12. Lunar & Planetary Laboratory, University of Arizona, Tucson, AZ 85721, USA
13. Department of Physics & Astronomy, University College Lond on, Gower Street, WC1E6BT, UK
14. Department of Astronomy and Astrophysics, University of Ch icago, 5640 S Ellis Ave, Chicago, IL 60637, USA
15. NASA Exoplanet Science Institute, California Institute of Technology, Jet Propulsion Laboratory, Pasadena, CA, USA
16. Spitzer Science Center, Infrared Processing and Analysis Center, California Institute of Technology, Mail Code 220-6, Pasadena, CA 91125, USA
17. Solar System Exploration Division, NASA Goddard Space Flight Center, Greenbelt, MD 20771, USA and
18. NASA Sagan Fellow

Submitted to ApJ April 24, 2017

ABSTRACT

We present observations of WASP-63b by the *Hubble Space Telescope (HST)* as part of "A Preparatory Program to Identify the Single Best Transiting Exoplanet for *JWST* Early Release Science". WASP-63b is one of the community targets under consideration for the *James Webb Space Telescope (JWST)* Early Release Science (ERS) program. We present a spectrum derived from a single observation by *HST* Wide Field Camera 3 in the near infrared. We engaged groups across the transiting exoplanet community to participate in the analysis of the data and present results from each. There is general agreement amongst all results that we find an H_2O absorption feature with 3.5–4.0σ significance. However, the feature is muted in comparison to a clear atmosphere at solar composition. Although the detection of the water feature is robust, the reasons for the muting of this feature are ambiguous due to a degeneracy between clouds and composition. The data does not yield robust detections of any molecular species other than H_2O. The group was motivated to perform an additional set of retrieval exercises to investigate an apparent bump in the spectrum at ~ 1.55 μm. We explore possible disequilibrium chemistry and find this feature is consistent with super-solar HCN abundance but it is questionable if the required mixing ratio of HCN is chemically and physically plausible. The ultimate goal of this study is to vet WASP-63b as a potential community target to best demonstrate the capabilities and systematics of *JWST* instruments for transiting exoplanet science. In the case of WASP-63b, the presence of a detectable water feature indicates that WASP-63b remains a plausible target for ERS observations.

Subject headings: planets and satellites: atmospheres – planets and satellites: individual: WASP-63b, techniques: spectroscopic, methods: numerical, atmospheric effects

1. INTRODUCTION

The *James Webb Space Telescope* will revolutionize transiting exoplanet atmospheric science due to a combination of its capability for continuous, long duration observations and its larger collecting area, spectral coverage, and resolution compared to existing space-based facilities. We previously outlined a plan in Stevenson et al. (2016) to fully demonstrate the capabilities of the *JWST* instruments during the Early Release Science (ERS) program allowing the community to plan more efficient and successful transiting exoplanet characterization programs in later cycles.

Stevenson et al. (2016) identified a set of "community targets" which meet a certain set of criteria for ecliptic latitude, period, host star brightness, well constrained orbital parameters, and predicted strength of spectroscopic features. WASP-63b was identified as one of the strongest transmission spectroscopy candidates for *JWST* Early Release Science. It is an inflated planet (1.43 R_J) with a low mass of only 0.38 M_J resulting in a large atmospheric scale height. It orbits a bright (11.2 V_{mag}) star. Additionally, WASP-63b occupies an important, underexplored, region of transmission spectroscopy due to its mass. Most exoplanets studied in detail with transmission spectroscopy are either hot Jupiters of mass ($\sim$1–3 M_J)(e.g. Deming et al. 2013; Kreidberg et al. 2014a, 2015a; Line et al. 2016; Sing et al. 2016) or Super Earth-to-Neptune mass planets ($\sim$0.01–0.1 M_J) (e.g. Kreidberg et al. 2014b; Fraine et al. 2014; Knutson et al. 2014). In order to understand formation and evolution processes, it's important to understand the composition of atmospheres over a full and continuous range of masses (e.g. Mordasini et al. 2016).

WASP-63b will be accessible to *JWST* approximately six months after the planned April 2019 start of Cycle 1 and ERS observations making it an ideal candidate should there be any delays in the *JWST* timetable. Here, we observe WASP-63b to evaluate its suitability as a prime candidate to test the capabilities of *JWST*. We can use the strength of the water absorption feature at 1.4 μm as a way to screen potential targets for the presence of obscuring aerosols and determine the amplitude of predicted spectral features (e.g. Deming et al. 2013; Kreidberg et al. 2014a; Sing et al. 2016; Stevenson 2016). Ideally, a clear atmosphere with large amplitude spectroscopic features will be best suited for benchmarking the instruments and identifying their systematics.

2. OBSERVATIONS AND ANALYSIS

We observed the WASP-63 system using the *HST* Wide Field Camera 3 (WFC3) on September 19, 2016. The observations were taken as part of program GO-14642, (PI Stevenson). The observations were made using the G141 grism in forward/reverse spatial scan mode. Spatial scanning (McCullough & MacKenty 2012) involves slewing the telescope in the cross dispersion direction during the exposure. In forward/reverse mode the telescope is exposing in both directions of the slew thus eliminating time to reset the target at the initial position on the detector between exposures. Each exposure, utilizing SPARS10, consists of 16 non-destructive reads with a total exposure time of approximately 103s which yielded peak per pixel counts near 32,000 electrons. The spectrum was read out using the 256 × 256 subarray with a scan rate of $\sim$ 0.08 arcsec/s (0.62 pixels/s). This corresponds to a total scan length of $\sim$ 8.76 arcsec which spreads the spectrum in the cross dispersion direction over $\sim$ 70 pixels. We observed WASP-63 for a total of 8 *HST* orbits to cover the entirety of the relatively long duration of transit ($\sim$ 5 hours).

We use the *IMA* files from the CalWF3 pipeline in our analysis. These files have been calibrated for dark current and zero read bias. We applied flat field corrections to each non-destructive read (NDR). Each NDR was background subtracted by considering a background window consisting of ($\sim$50) rows of pixels adjacent to the spectrum. A mean value for each column of the background window was taken to produce a one-dimensional background correction. The 1-D solution was then smoothed in the dispersion direction to correct for outliers. The column by column background value was then subtracted from each pixel of the image. We then extract the spectrum by taking the difference between successive NDRs. We apply a top hat filter to each NDR to limit any contribution from cosmic rays and/or overlapping spectra (Evans et al. 2016; Wakeford et al. 2017). The differences between each NDR are then summed to produce a final working image.

2.1. *Band Integrated Light Curve*

We perform the extraction of the band integrated light curve (white light curve) using a range of different aperture sizes in the cross-dispersion direction. Each orbit includes a direct image of the star. The trace and wavelength solutions are calculated from the centroid of the undispersed image using the coefficients provided in Kuntschner et al. (2009). We extract a box from each working image with the number of columns corresponding to wavelength limits 1.125-1.65 μm and rows determined by the chosen aperture size. The band integrated light curve is the summation of all pixels within the box at each time step. The results of the initial extraction of the raw white light curve are shown in Figure 1 (top).

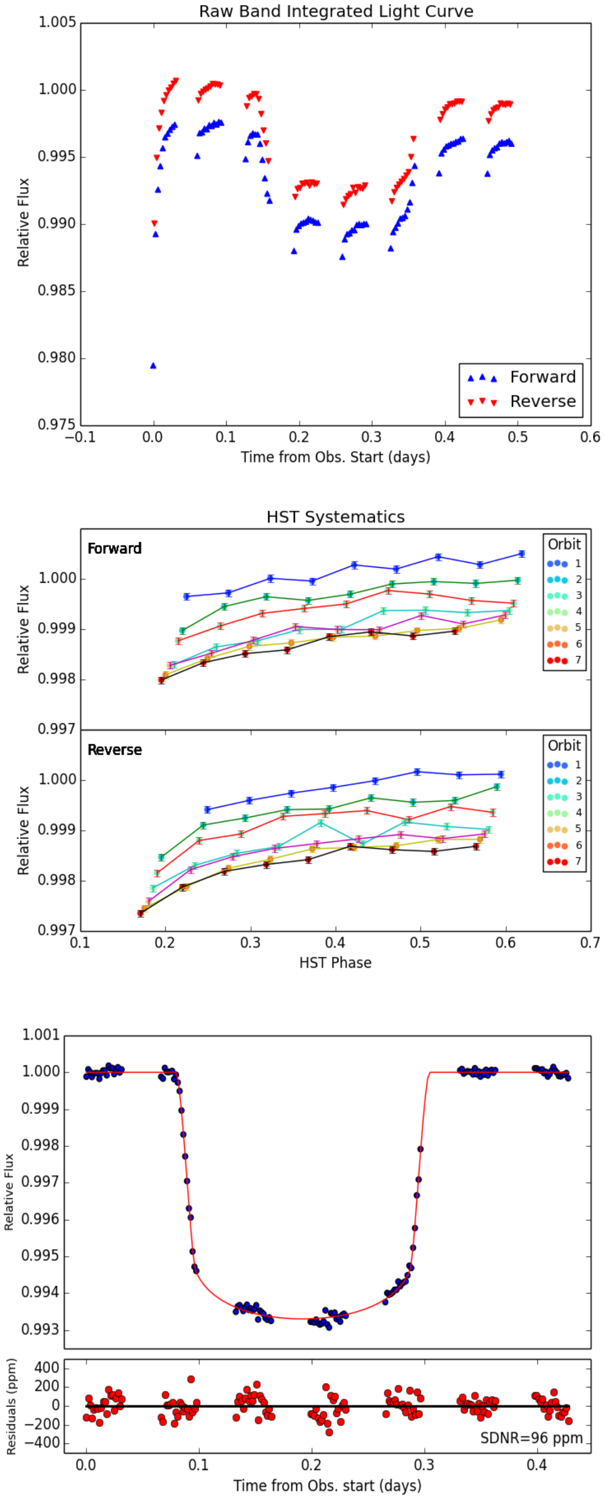

FIG. 1.— *Top:* The normalized raw band integrated light curve. Forward/Reverse scans are shown in red/blue. *Middle:* The Band Integrated Light Curve phase folded by *HST* Orbital Phase after removing the best fit transit model to illustrate the systematic 'hook' in WFC3 observations. The forward and reverse scan directions are shown in separate panels. Each color corresponds to an *HST* orbit. The exponential increase over each orbit and a visit long decrease in response are evident by visual inspection. *Bottom:* The best fit white light curve shown with systematics removed. We achieve a standard deviation of the normalized residuals of 96 ppm.

TABLE 1
BEST FIT VALUES AND UNCERTAINTIES FOR EPHEMERIDES FROM BAND INTEGRATED LIGHT CURVE FIT.

$R_p/R_\star$	$T_{cen}(MJD)$	$a/R_\star$	i (°)
$0.077762\pm^{0.000204}_{0.000183}$	$57650.435\pm^{6.97\times10^{-5}}_{5.93\times10^{-5}}$	$6.633\pm^{0.031}_{0.015}$	$88.52\pm^{0.26}_{0.12}$

Fitting the white light curve requires accounting for *HST* systematics. We choose to follow the standard practice of discarding the first orbit as it presents different systematics from the remainder of the data (e.g. Deming et al. 2013; Stevenson et al. 2014). The raw light curve exhibits a ramp like increase in flux, commonly referred to as the 'hook', with each *HST* orbit consistent with previous observations (e.g. Berta et al. 2012; Deming et al. 2013; Fraine et al. 2014; Kreidberg et al. 2014a). The hook effect, shown in Figure 1 (middle), is generally steeper in the first frame of each *HST* orbit so we discard those data points. We then model the hook *HST* systematics as an exponential plus linear function of the form $1 - A\exp\{S(\theta - \theta_0)\} + c_1\theta$ where θ is the *HST* orbital phase, θ_0 is a reference angle for setting zero *HST* phase and A, S, c_1,c_2 are scaling factors. The hook model is combined with a second order polynomial in time over the entirety of the observation.

We model the transit using the methods of Mandel & Agol (2002) implemented by the Python routine BATMAN Kreidberg (2015). Orbital parameters used for the transit model were taken from Hellier et al. (2012). We calculate non–linear limb darkening coefficients using the PHOENIX Code to fit theoretical spectra as described in detail in de Wit et al. (2016). During the fitting process we allow for the time of transit center (T_{cen}), planetary radius as a fraction of stellar radius ($R_p/R_\star$), $a/R_\star$, inclination (i), and a normalizing factor for each of the scan directions to be free parameters and fit both scan directions simultaneously. All fits and uncertainty estimates are derived from the Python routine 'emcee' (Foreman-Mackey et al. 2013). We choose the best aperture by minimizing the scatter of the residuals of the white light curve fit. We find a best aperture of ± 44 pixels in the spatial direction centered on the spectral image centroid. We achieve a standard deviation of the normalized residuals (SDNR) of 96 parts per million (ppm). The best fit white light curve is shown in Figure 1 (bottom) and the values and uncertainties for ephemerides from the best fit white light curve are presented in Table 1.

2.2. *Spectral Light Curves*

The spectral light curves are extracted using the same aperture we found to minimize the SDNR of the white light curve. The range of wavelengths included in our aperture are divided into 15 bins of width 0.035 μm. The spectrum from each frame is compared to the spectrum of the first frame using cross correlation in Fourier space to check for any shift in the wavelength–pixel solution. The shift in wavelength solution throughout the observation was on the order of a few tenths of a pixel. Each column was summed and weighted by the fraction of that pixel in the bin.

The systematics were removed from the spectral light curves using the divide white method (Deming et al. 2013; Kreidberg et al. 2014a; Stevenson et al. 2014). Removing the best fit transit from the white light curve leaves only the systematics. We divide each spectral light curve by the systematics. This assumes that the systematics are wavelength independent. We do note a linear, observation–long, wavelength dependence in the corrected spectral light curves. We use a first order polynomial to account for the wavelength dependent systematics combined with the transit model when fitting the spectral light curves. We fix ephemerides to the white light curve solutions and use fixed, wavelength dependent, non-linear limb darkening coefficients derived in the same way as described in Section 2.1. The transit depth and normalization factors are left as the only free parameters. We fit both scan directions simultaneously. Spectral light curves and their fits are shown in Figure 2.

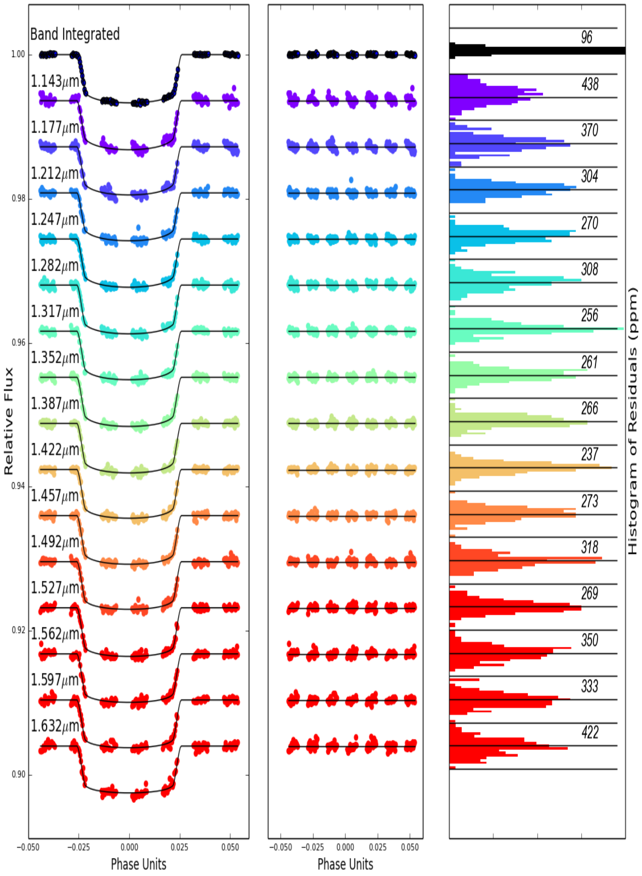

FIG. 2.— *Left:* Spectrophotometric transit light curves (colored dots) with systematics removed compared with the best fit transit (solid line). Light curves are shown as orbital phase (0-1 with 0 as the center of transit) vs. relative flux (vertically shifted for clarity). Each light curve is labeled with the central wavelength of the spectral bin. *Center:* Residuals to the fit. *Right:* Normalized histograms of the residuals. The solid black horizontal lines are spaced at 1000 ppm intervals for scale and the SDNR of each fit is listed in units of ppm.

2.3. *Transmission Spectrum*

A transmission spectrum was derived from the transit depth fits of the spectral light curves. The change in the apparent planetary radius as a function of wavelength can be indicative of absorption features of molecular species in the planetary atmosphere. As a test for robustness, the spectrum of

TABLE 2
TRANSMISSION SPECTRUM OF WASP-63B MEASURED WITH *HST* WFC3 G141 GRISM.

Wavelength(μm)	$R_p/R_\star$	Uncertainty (ppm)
1.1425	0.07791	310
1.1775	0.07732	290
1.2125	0.07717	300
1.2475	0.07753	300
1.2825	0.07812	280
1.3175	0.07789	270
1.3525	0.07847	290
1.3875	0.07891	300
1.4225	0.07832	290
1.4575	0.07839	300
1.4925	0.07773	330
1.5275	0.07865	330
1.5625	0.07866	370
1.5975	0.07816	350
1.6325	0.07751	360

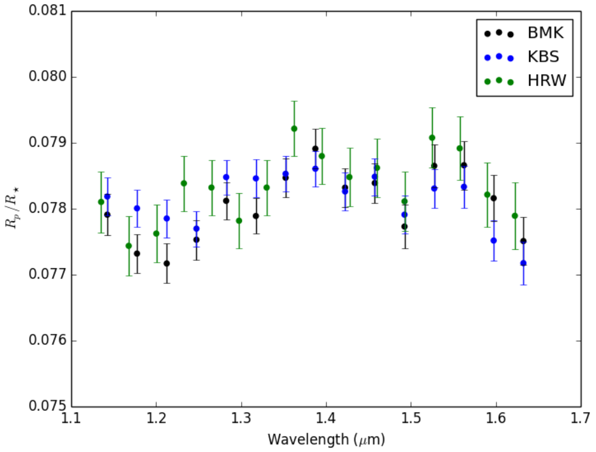

FIG. 3.— Results of spectral extraction from multiple independent analyses show good agreement. Here we show the best fit value for $R_p/R_\star$ as a function of wavelength with 1σ error bars derived from the MCMC posteriors. Colors correspond to analysis performed by Brian Kilpatrick (BMK), Kevin Stevenson (KBS), and Hannah Wakeford (HRW).

WASP-63b was extracted using multiple independent analysis pipelines in addition to the method described in detail in the previous subsections. Figure 3 shows a comparison of the results from this methodology (BMK) with that of analysis performed using methods described in Stevenson et al. (2014) (KBS) and Wakeford et al. (2016, 2017) (HRW). Results from the spectral extraction performed by BMK are listed in Table 2.

3. RESULTS

The results presented in Table 2 were distributed to the members of the transiting exoplanet community who were involved with the preparation of Stevenson et al. (2016) and/or *HST* program GO 14642. Each was given an opportunity to provide an independent analysis of the results. Wide community involvement resulted in a number of contributions in the form of forward model comparisons and retrievals. Here we present the methods and findings from each interpretation of the spectrum.

3.1. *Forward Models*

3.1.1. *Burrows*

We apply the transit models from Howe & Burrows (2012), which adopt chemical equilibrium abundances for molecular species from Burrows & Sharp (1999) and opacities from Sharp & Burrows (2007). The atmospheric models consider an isothermal temperature profile and gray haze opacity with cross sections of 0.001–0.005 $\mathrm{cm}^2\mathrm{g}^{-1}$ from 10^{-6} bar to 1 bar.

By exploring a range of temperatures, haze opacities, metallicities, and non-equilibrium CO/CH_4 abundances, the best-fitting solutions pointed to solar-abundance atmospheres at a temperature of 1000 K, with a haze/cloud muting the water absorption feature at 1.4 μm (Figure 4, top panel). There is no indication of significant CH_4. There is a slight degeneracy between the cloud thickness and temperature, but it is clear that the atmosphere is cloudy. These models do not show a significant metallicity dependence. Finally, a high CO abundance excess ($\sim$100 times solar) can help to fit the data at 1.5 μm, but it does not seem realistic.

3.1.2. *Heng*

As a complementary approach to the full retrieval calculations, we fit the data with a 3-parameter analytical model (Heng & Kitzmann 2017). In that study, it was demonstrated that this isothermal, isobaric model matched full numerical calculations at the $\sim 0.1\%$ level over the WFC3 wavelength range. The model has three parameters: temperature, water abundance, and a constant cloud opacity. The constant cloud opacity assumes that the cloud particles are large over the wavelength range probed by WFC3 (i.e., micron-sized or larger radius). Water opacities are computed using the HELIOS-K opacity calculator (Grimm & Heng 2015) and the HITEMP spectroscopic database. This procedure confronts the data with a simple model, which has a minimal number of parameters, to serve as a plausibility check.

For WASP-63b, we adopt a white-light radius of 1.43 Jupiter radii and a surface gravity of 417 cm s^{-2} (Hellier et al. 2012). Following the approach of Kreidberg et al. (2015b), we equate the reference transit radius to the white-light radius and set the reference pressure to 10 bar. We assume a hydrogen-dominated atmosphere and set the mean molecular weight to 2.4. The top panel of Figure 4 shows the best-fit model to the WFC3 WASP-63b data. Our general conclusion mirrors that of the retrieval calculations: water is present in the atmosphere of WASP-63b, but its presence is muted by a continuum, which in this case is attributed to a constant cloud opacity. The values of our fitting parameters span a temperature range from 500 to 1000 K, a water mixing ratio from $\sim 10^{-8}$ to 10^{-7}, and a cloud opacity $\sim 10^{-8}$ to 10^{-7} cm^2 g^{-1}.

3.1.3. *Morley*

In order to determine the clouds that are predicted to form in the atmosphere of WASP-63b and their effect on the planet's transmission spectrum, we ran self-consistent models including the effects of cloud condensation. These models solve for the temperature structure of the atmosphere in radiative-convective and chemical equilibrium and are more extensively described in McKay et al. (1989); Marley et al. (1996); Burrows et al. (1997); Marley et al. (1999, 2002); Fortney (2005); Saumon & Marley (2008); Fortney et al. (2008); Morley et al. (2015). Our opacity database for gases is described in Freedman et al. (2008, 2014), and we calculate the effect of cloud opacity using Mie theory, assuming spherical particles. We include iron and silicate clouds and vary the cloud sedimentation efficiency $f_{\rm sed}$ from 0.1 to 1, and find that these clouds do indeed form at high altitudes and damp the size of the signal for low sedimentation efficiencies (i.e. lofted clouds of small particles). Figure 4 top panel shows a representative transmission model for WASP-63b.

3.1.4. *Parmentier*

In order to understand how the three-dimensional structure of the planet might affect our interpretation of the planet's transmission spectrum, we model WASP-63b with the three-dimensional global circulation model SPARC/MITgcm described in Showman et al. (2009). Our model solves for the three-dimensional temperature structure of the atmosphere assuming a cloud-free, solar-composition atmosphere. We then use the temperature map to predict the position of the clouds at the limb of the planet by comparing the partial pressure and the saturation pressure of the cloud gaseous constituents as described in Parmentier et al. (2016). The cloud top level and size of the cloud particles are free parameters representing vertical mixing and microphysics respectively. We then compute the transmission spectrum of the whole atmosphere by combining the transmission spectrum obtained with the temperature and cloud profile at each latitude around the limb.

Our global circulation model predicts a temperature difference of 400K between the east and west limb at the 10 mbar level. As a consequence some cloud species are predicted to be condensed all over the limb of the planet whereas others should condense only on the morning limb and be evaporated on the other one, leading to a partially cloudy atmosphere (Line et al. 2016). We computed models assuming the presence of enstatite clouds ($MgSiO_3$) or manganese sulfide clouds (MnS) corresponding to a fully cloudy and partially cloud case respectively. Our best fit spectrum with enstatite clouds is very similar to the Morley model of Fig.4. It has a cloud top pressure of 1 mbar and no constraints on the particle size. Our best fit model with MnS clouds is the Parmentier model of Fig. 4. It has a limb that is ≈ 60% cloudy, resulting in a qualitatively different spectrum than the other, one-dimensional models shown here. For this model the cloud top pressure is $\approx 0.1 mbar$ and the particle size is $\approx 1 \mu m$. We conclude that the atmosphere of WASP-63b is unlikely to be clear with a solar-composition abundance of water. Both fully cloudy and partially cloudy atmospheres can exist, depending on the cloud composition. A higher signal to noise spectrum should be able to disentangle between the two scenarios.

3.2. *Retrievals*

Four groups provided atmospheric retrieval analyses for WASP-63b. The following subsections describe the retrieval procedure and the individual exploration from each group. Figures relative to the individual retrievals are included in the Appendix.

3.2.1. *Blecic & Cubillos*

To model the atmosphere and spectrum of WASP-63b we use the Python Radiative Transfer in a Bayesian framework (Pyrat Bay) package[1] (Cubillos et al. 2017, in prep.; Blecic et al. 2017, in prep.). Pyrat Bay is an open-source reproducible code, based on the Bayesian Atmospheric Radiative Transfer package (Blecic 2016; Cubillos 2016). The code provides a line-by-line radiative-transfer and a thermochemical-equilibrium abundances (TEA, Blecic et al. 2016) module, which can be use in forward or retrieval mode, via a Differential-evolution MCMC sampler (Cubillos et al. 2017).

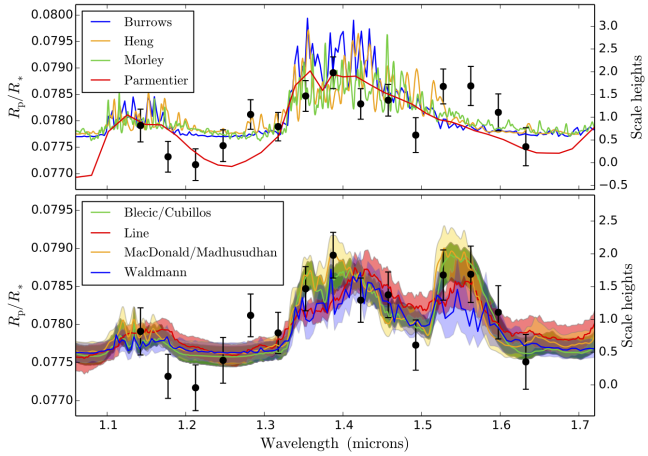

FIG. 4.— *Top:* WASP-63b spectrum and forward models. The black dots with error bars denote the observed best-fit radius ratio and 1σ uncertainties. The labeled solid curves show representative forward model fits to the data described in section 3.1. *Bottom:* WASP-63b spectrum and retrieval models including HCN absorption. The black dots with error bars denote the observed best-fit radius ratio and 1σ uncertainties. The labeled solid curves denote the best-fitting models for the consistent retrieval run described in section 4. The vertical shaded areas around each model denote the span of the 1σ confidence region of the posterior distribution of sampled models.

To model the transmission spectra of WASP-63b, Pyrat Bay considers molecular opacities for H_2O (HITEMP, Rothman et al. 2010), NH_3 and CH_4 (HITRAN, Rothman et al. 2013), and HCN (Exomol, Barber et al. 2014); collision induced absorption from H_2-H_2 (Borysow et al. 2001; Borysow 2002) and H_2-He (Borysow et al. 1988, 1989; Borysow & Frommhold 1989); and H_2 Rayleigh scattering (Lecavelier Des Etangs et al. 2008).

The atmospheric model consist of a 1D set of concentric shell layers in hydrostatic equilibrium. For the temperature profile we consider the three-channel Eddington approximation parameterization (TCEA, Line et al. 2013b) or an isothermal profile. We also consider two cloud parameterizations, a simple gray-cloud opacity with constant cross section (cm^{-2} $molec^{-1}$) below 10^{-5} bars, and a thermal-stability cloud model based on the approach described in Ackerman & Marley (2001) and Benneke (2015), with additional flexibility (Blecic et al. 2017, in prep). We compute the opacity from either Fe and $MgSiO_3$ condensates using Mie-scattering theory (Toon & Ackerman 1981), parameterizing the cloud profile shape, condensate mole fraction, particle-size distribution, and gas number fraction just below the cloud deck.

We explored several cases considering free parameters for the abundances of H_2O, NH_3, CH_4, and HCN (constant vertical profiles), the planetary radius at 0.1 bar, and the temperature and cloud models described above. We obtained qualitatively good fits with free abundances in either the gray-cloud, complex-cloud, and clear cases. As expected for transmission spectroscopy, the retrieval returned largely unconstrained pa-

---

[1] http://pcubillos.github.io/pyratbay

rameters for the TCEA temperature model, suggesting that the data does not justify for more complex models than an isothermal profile. In all cases the MCMC favors lower temperatures ($T < 1000$ K) than equilibrium temperature (1500 K) at the pressures probed by the observations. We constrain the water abundance, ranging from solar to $\sim$0.1 times solar values. The observed water absorption feature is muted relative to a clear atmosphere with solar abundances. This is caused by a sub-solar water abundance, an absorbing cloud opacity, or a high mean molecular mass, which reflects in a strong correlation between the water abundance and the cloud cross-section. When we compare retrievals with the gray and complex cloud model, we find similar best-fitting spectra between the two cases. The complex-cloud retrieval does not constrain any of the cloud parameters when we set all four species abundances free. In the case when we set the water abundance as the only abundance free parameter, we find a somewhat better condensate-fraction constraint. Since the cloud opacity dominates only a limited region of the observed spectrum ($\sim$1.2–1.3 μm), we conclude that there is no need for a more complex cloud model for this study.

3.2.2. *Line*

We use the CHIMERA transmission model (Line et al. 2013a; Swain et al. 2014; Kreidberg et al. 2014a, 2015b; Greene et al. 2016; Line et al. 2016). For transit geometry, the code solves the radiative-transfer equation for parallel rays across the terminator of the planet (Brown 2001; Tinetti et al. 2012). The code integrates atmospheric opacities from either correlated-K or sampled “line-by-line" absorption cross sections Freedman et al. (data from 2014).

The atmosphere uses ’thermochemically-consistent’ molecular abundances (as defined in Kreidberg et al. (2015b)), computed using the NASA CEA2 model for given elemental abundances (Lodders 2009). The elemental abundances are parameterized by the metallicity [M/H], the carbon-to-oxygen ratio log(C/O), and the carbon- and nitrogen-species quench pressures (Kreidberg et al. 2015b; Morley et al. 2017). The temperature profile comes from the radiative-equilibrium model from Guillot (2010). The model includes a power law haze, (Lecavelier Des Etangs et al. 2008) and an opaque gray patchy cloud model parameterized by the top-pressure boundary and a ’Patchy terminator’ parameter (Line & Parmentier 2016). The atmosphere is in hydrostatic equilibrium with height-dependent gravity, temperature, and molecular weight. A radius scale factor sets the reference altitude at 10 bars. To explore the parameter space, the transmission model is coupled with the PyMultiNest (Buchner et al. 2014) multimodal nested-sampling algorithm (Feroz & Hobson 2008).

The ’chemically-consistent’ retrieval detects the water spectral feature at 3.6σ confidence. There is no evidence for spectroscopic features from other species.

This is consistent with a hard upper limit on C/O near 1. The water band is muted relative to solar composition. The retrieval posterior shows two ’composition’ modes: low metallicity ([M/H] $\lesssim$ 1.3 (20×)) degenerate with a cloud and high metallicity (peak near $\sim$300×solar). There is a turn-over degeneracy in cloud top vs. [M/H] (due to the effect on the mean molecular weight) resulting in the bi-modal marginalized metallicity distribution. Clouds can be present, but are not required to fit the spectra as given by the Bayes factor (0.45) and result in a much lower value for the low metallicity mode (<0.1×solar), while the high metallicity mode remains.

The highest of the sampled metallicities (greater than $\sim$50 times solar) are possibly implausible given mass and radius of WASP-63b.

Further tests found negligible variations when imposing a temperature prior or no patchy-cloud factor. A comparison between correlated-K and line-by-line sampling opacities produced nearly identical results. Likewise, a more complex, Mie-cloud model (Lee et al. 2013) produced qualitatively similar main conclusions (with unconstrained cloud particle sizes, vertical extent, or cloud composition).

3.2.3. *MacDonald & Madhusudhan*

We use the nested-sampling retrieval algorithm POSEIDON (MacDonald & Madhusudhan 2017) to analyze the WFC3 observations of WASP-63b. To compute detection significances we conduct nested Bayesian model comparisons. For simplicity, we assume an isothermal temperature-pressure profile, consider molecular opacities due to H_2O, CH_4, NH_3, and HCN, and model clouds as a uniform-in-altitude gray opacity. We model the atmosphere of WASP-63b with 100 layers uniformly spaced in log-pressure between $10^{-6} - 10^2$ bar with a surface gravity of $g = 4.1687$ m s^{-2}. We assume a hydrogen and helium-dominated composition with ratio He/H_2 = 0.17. The retrieval free parameters are the temperature, the reference pressure, the mixing ratio of H_2O, CH_4, NH_3, and HCN, and the gray opacity.

The model comparison test marginally prefer the gray-opacity case ($\chi^2_{\rm red} = 1.21$) over a cloud-free case ($\chi^2_{\rm red} = 1.46$), with a Bayes factor of 2.2. Adopting the gray-opacity model, we detect H_2O at 4.0σ (Bayes factor = 601), HCN at 3.1σ (Bayes factor = 27.6), and ’nitrogen chemistry’ (combination of HCN and NH_3) at 3.3σ (Bayes factor = 53.7). We do not detect CH_4.

3.2.4. *Waldmann*

We retrieved the *HST* /WFC3 spectrum of WASP-63b using the Tau-REx atmospheric retrieval framework (Waldmann et al. 2015b,a; Waldmann 2016). Based on the Tau code transmission forward models by Hollis et al. (2013), Tau-REx employs Nested Sampling (Feroz & Hobson 2008) to solve the full Bayesian argument. Molecular line list opacities were obtained from the ExoMol project (Tennyson & Yurchenko 2012), HITRAN (Rothman et al. 2009, 2013) and HITEMP (Rothman et al. 2010). Rayleigh scattering and collision induced absorption of H_2-H_2 and H_2-He (Borysow et al. 2001; Borysow 2002) was also included. Tau-REx can use high-resolution absorption cross-section or correlated-k tables as opacity inputs. Here we used the latter but find both to yield equivalent results for the wavelength ranges and sensitivities of the data at hand. We include pressure-dependent line broadening where such information is available, taking into account the J quantum number dependence on pressure broadening coefficients. We model clouds using a hybrid model of gray-cloud opacities and a phenomenological Mie scattering model (Lee et al. 2013). In this study, we assume an isothermal temperature-pressure profile of the atmosphere.

We run two types of retrievals, a ’free’ retrieval with planet radius, temperature, cloud-top pressure and abundances of H_2O, CH_4, CO, CO_2, NH_3 as free parameters, as well as a chemical-equilibrium model retrieval using an implementation of the ACE model by Agúndez et al. (2012). Here, the free parameters are the C/O ratio, atmospheric metallicity, planet radius, temperature and cloud-top pressure. We detect water with a 3.5σ significance (Bayes factor = 103)

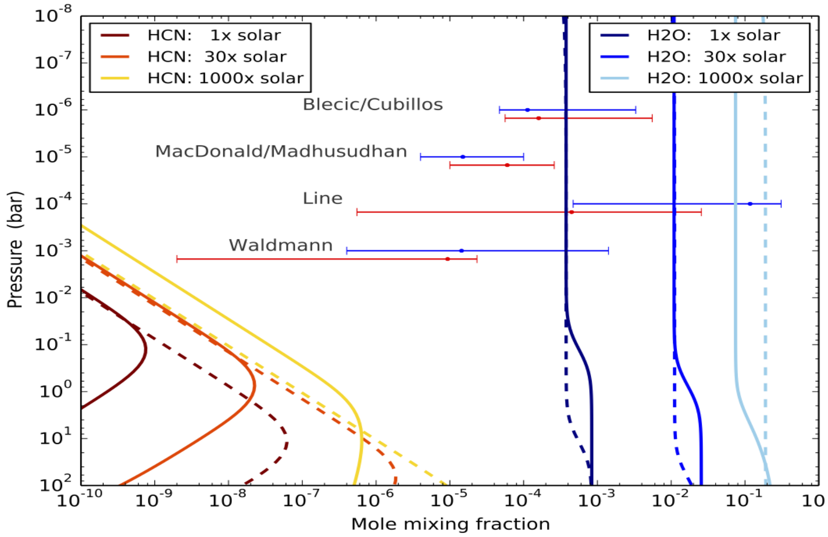

FIG. 5.— Water and HCN abundances for WASP-63b compared to thermochemical-equilibrium mole mixing fractions models for an isothermal atmosphere at 1000 K (solid lines) and at 1500 K (dashed lines) at a range of metallicities (see labels). The horizontal error bars show the retrieved 68% credible-region abundances from each group (labels) for water (blue) and HCN (red). **Note that the retrieved abundances are vertically offset for clarity.** All abundances correspond to the pressure levels probed by this transmission observation (10^{-2}–10^{-4} bar). All retrieved water abundances are consistent with solar or slightly sub-solar water abundances, however the retrieved HCN values range several order of magnitudes higher than any 1000 K equilibrium value. The retrieved mole mixing fractions of HCN are more plausible if the temperature at deeper layers were ~1500 K and vertical transport dominated the abundances in the region probed by observations. The models suggest it would be possible under these conditions to produce mole mixing fractions on the order of 10^{-6}.

compared with a family of pure-cloud or featureless atmosphere models. We obtain $\log(\mathrm{H_2O}) = -4.84^{+1.04}_{-1.53}$. We do not find any evidence of an extended Rayleigh curve due to hazes but found a gray-cloud model to be sufficient. We constrain the cloud-top pressure to $\log(p) = 3.08^{+1.48}_{-0.93}$ Pa. The chemically consistent retrieval yielded two results. The first result yields a high metallicity atmosphere at 370 times solar. The second result yields a low metallicity atmosphere at 0.24 times solar. Both solutions feature comparable log-evidences and result in upper bounds of C/O at 0.49. A ratio of $\mathrm{C/O} < 0.7$ is expected as only water is retrieved in this data set and is therefore consistent with the 'free' retrieval approach above. The atmospheric metallicity is poorly constrained due to the presence of clouds which has the effect of muting the water feature and biasing the chemical-consistent model to either compensate with unrealistically high mean molecular weight atmospheres or unrealistically low trace gas abundances.

4. DISCUSSION

The individual atmospheric analyses of WASP-63b agree that there is a robust water detection (3.5–4.0 σ), but with a muted absorption feature when compared to a clear solar-composition atmospheric model. It is unclear if the reason for the muting of the feature is the result of sub-solar water abundance, absorbing cloud opacity, or a high mean molecular mass. Thermochemically-consistent retrievals show a multimodal solution due to degeneracies between cloud opacity and composition (Figures: 7 and 9). Retrievals with simple temperature (isothermal) and cloud (gray opacity) models both produced fits consistent with retrievals with more complex models and thus the data does not warrant the incorporation of more complex models nor does it allow further constraints on cloud properties.

The high transit-depth values between 1.5 and 1.6 μm motivate the inclusion of HCN and the exploration of disequilibrium chemistry. Each retrieval team performed an additional retrieval exercise with a common set of assumptions to further explore the the inclusion of HCN as a means to fit the 'bump' in the spectrum between 1.5 and 1.6 μm. We implemented an isothermal temperature model, a gray-opacity cloud model, a free pressure–radius reference point, and opacities from H_2-Rayleigh, H_2-H_2 and H_2-He CIA, and H_2O, CH_4, HCN, and NH_3. We adopted molecular abundances either from thermochemically-consistent calculations or from free abundances (constant vertical profiles), with the exception of the HCN abundance, which is always a free fitting variable (constant vertical profile).

We begin with this common set of assumptions and then compare retrieval results from teams with differing retrieval frameworks. Notable differences include: the statistical sampler from Blecic/Cubillos (MCMC) differ from the rest (Nested sampling), the molecular opacity handling from Waldmann and Line (correlated-K) differ from the others (cross-section sampling), and the chemistry from Line (thermochemically-consistent) differs from the rest (free constant vertical profiles). Figure 4 shows the retrieved spectrum from the run using the common assumptions. All four retrievals produced consistent spectral fits, seen in the intersecting 68% confidence regions around the best-fitting models. In terms of the atmospheric characterization, these retrievals confirm the previously found water detection.

The Bayesian hypothesis testing favors the fit with HCN, improving the fit at 1.5–1.6 μm. However, the detection significance is low and inconsistent, 3.1σ (Blecic/Cubillos), 2.1σ (Line), 3.1σ (MacDonald/Madhusudhan), and 1.9σ (Waldmann). Therefore, for the currently available data, the inclusion of HCN is not statistically justified within this model parameterization. Furthermore, to reproduce the observed values requires the HCN mole fraction be $\gtrsim 10^{-5}$; much higher than thermochemical-equilibrium values (Figure 5). To produce such high HCN abundances, one would need to invoke disequilibrium-chemistry processes by either quenching or photochemistry. Quenching can occur when higher temperatures at deep layers, below the levels probed by this observation, enhance the HCN abundance without needing the high metallicities from Figure 5. If vertical mixing dominates the mid-altitude abundances of the WASP-63b atmosphere (expected at the retrieved temperatures of $\sim$1000 K), HCN could be effectively quenched, maintaining the high abundances from the deep layers throughout the probed region. Similar deviations from equilibrium chemistry have been modeled for other Jupiter-like exoplanets (Moses et al. 2011; Venot et al. 2012). None of the retrievals constrain any of the other molecular abundances that could provide additional evidence for quenching (e.g. CO, CH_4, NH_3). However, photochemistry could play a role in removing these other molecules from the atmosphere while enhancing the mole fraction of HCN at pressures less than a millibar. Moses et al. (2011, 2013) show that ammonia and methane can be photochemically converted to HCN at the pressure levels probed by near–IR transmission spectroscopy thus driving the retrieved abundances much higher than equilibrium values. Future observations with extended wavelength ranges and higher sensitivity, such as *JWST* , can help to definitively confirm or rule out the detection of HCN, and other atmospheric species, thus constraining the presence of disequilibrium chemistry.

5. CONCLUSIONS

We present the observations of one transit of the hot Jupiter WASP-63b. Observations were conducted in the near-infrared using *HST* WFC3 G141. This study was done as a preliminary evaluation of the suitability of WASP-63b as one of the community targets for *JWST* ERS science. We have detected a muted water absorption feature at $\sim$ 1.4 μm confirming WASP-63b as a potential target for ERS science. The potential presence of an absorption feature at 1.55μm is not evidence enough to make strong conclusions about the presence of other molecules in the atmosphere, however, further observations by *JWST* would be able to identify additional spectral features that would allow us to further constrain the atmospheric composition. The observational window for observing WASP-63b with *JWST* is from September 23 – April 5. *JWST* is currently scheduled to launch in October 2018 and ERS observations would commence in April 2019. Assuming the mission remains on schedule, WASP-63b would not be observable until several months after the ERS program window. However, if there are any delays to launch or the start of ERS observations, WASP-63b would be a prime candidate for study with multiple instruments and modes.

6. ACKNOWLEDGMENTS

This work is based on observations made with the NASA/ESA Hubble Space Telescope, obtained from the Data Archive at the Space Telescope Science Institute, which is operated by the Association of Universities for Research in Astronomy, Inc., under NASA contract NAS 5-26555. These observations are associated with program GO-14642. BMK acknowledges funding by HST-GO-14642.047 provided by the Space Telescope Science Institute. The authors acknowledge the contributions and support from members of the transiting exoplanet community who have contributed to and/or supported Program GO-14642 including: E. Agol, D. Angerhausen, T. Barman, J. Barstow, N. M. Batalha, S. Birkman, D. Charbonneau, N. Cowan, N. Crouzet, S. Curry, J. M. Desert, D. Dragomir, J. Fortney, A. Garcia Munoz, N. Gibson, J. Gizis, T. Greene, J. Harrington, T. Kataria, E. Kempton, H. Knutson, L. Kreidberg, M. Lopez-Morales, M. Rocchetto, E. Schlawin, E. Shkolnik, A. Shporer, D. Sing, K. Todorov, and J. de Wit.

REFERENCES

Ackerman, A. S., & Marley, M. S. 2001, ApJ, 556, 872
Agúndez, M., Venot, O., Iro, N., et al. 2012, A&A, 548, A73
Barber, R. J., Strange, J. K., Hill, C., et al. 2014, MNRAS, 437, 1828
Benneke, B. 2015, ArXiv e-prints
Berta, Z. K., Charbonneau, D., Désert, J.-M., et al. 2012, ApJ, 747, 35
Blecic, J. 2016, ArXiv e-prints
Blecic, J., Harrington, J., & Bowman, M. O. 2016, ApJS, 225, 4
Borysow, A. 2002, A&A, 390, 779
Borysow, A., & Frommhold, L. 1989, ApJ, 341, 549
Borysow, A., Frommhold, L., & Moraldi, M. 1989, ApJ, 336, 495
Borysow, A., Jorgensen, U. G., & Fu, Y. 2001, J. Quant. Spec. Radiat. Transf., 68, 235
Borysow, J., Frommhold, L., & Birnbaum, G. 1988, ApJ, 326, 509
Brown, T. M. 2001, ApJ, 553, 1006
Buchner, J., Georgakakis, A., Nandra, K., et al. 2014, A&A, 564, A125
Burrows, A., & Sharp, C. M. 1999, ApJ, 512, 843
Burrows, A., Marley, M., Hubbard, W. B., et al. 1997, ApJ, 491, 856
Cubillos, P., Harrington, J., Loredo, T. J., et al. 2017, AJ, 153, 3
Cubillos, P. E. 2016, ArXiv e-prints
de Wit, J., Wakeford, H. R., Gillon, M., et al. 2016, Nature, 537, 69
Deming, D., Wilkins, A., McCullough, P., et al. 2013, ApJ, 774, 95
Evans, T. M., Sing, D. K., Wakeford, H. R., et al. 2016, ApJ, 822, L4
Feroz, F., & Hobson, M. P. 2008, MNRAS, 384, 449
Foreman-Mackey, D., Hogg, D. W., Lang, D., & Goodman, J. 2013, PASP, 125, 306
Fortney, J. J. 2005, MNRAS, 364, 649
Fortney, J. J., Marley, M. S., Saumon, D., & Lodders, K. 2008, ApJ, 683, 1104
Fraine, J., Deming, D., Benneke, B., et al. 2014, Nature, 513, 526
Freedman, R. S., Lustig-Yaeger, J., Fortney, J. J., et al. 2014, ApJS, 214, 25
Freedman, R. S., Marley, M. S., & Lodders, K. 2008, ApJS, 174, 504
Greene, T. P., Line, M. R., Montero, C., et al. 2016, ApJ, 817, 17
Grimm, S. L., & Heng, K. 2015, ApJ, 808, 182
Guillot, T. 2010, A&A, 520, A27
Hellier, C., Anderson, D. R., Collier Cameron, A., et al. 2012, MNRAS, 426, 739
Heng, K., & Kitzmann, D. 2017, ArXiv e-prints
Hollis, M. D. J., Tessenyi, M., & Tinetti, G. 2013, Computer Physics Communications, 184, 2351
Howe, A. R., & Burrows, A. S. 2012, ApJ, 756, 176
Knutson, H. A., Benneke, B., Deming, D., & Homeier, D. 2014, Nature, 505, 66
Kreidberg, L. 2015, batman: BAsic Transit Model cAlculatioN in Python, Astrophysics Source Code Library
Kreidberg, L., Bean, J. L., Désert, J.-M., et al. 2014a, ApJ, 793, L27
—. 2014b, Nature, 505, 69
Kreidberg, L., Line, M. R., Bean, J. L., et al. 2015a, ApJ, 814, 66
—. 2015b, ApJ, 814, 66
Kuntschner, H., Bushouse, H., Kümmel, M., & Walsh, J. R. 2009, WFC3 SMOV proposal 11552: Calibration of the G141 grism, Tech. rep.
Lecavelier Des Etangs, A., Pont, F., Vidal-Madjar, A., & Sing, D. 2008, A&A, 481, L83
Lee, J.-M., Heng, K., & Irwin, P. G. J. 2013, ApJ, 778, 97
Line, M. R., Knutson, H., Deming, D., Wilkins, A., & Desert, J.-M. 2013a, ApJ, 778, 183
Line, M. R., & Parmentier, V. 2016, ApJ, 820, 78
Line, M. R., Wolf, A. S., Zhang, X., et al. 2013b, ApJ, 775, 137
Line, M. R., Stevenson, K. B., Bean, J., et al. 2016, AJ, 152, 203
Lodders, K. 2009, Exoplanet Chemistry (Wiley-VCH)
MacDonald, R. J., & Madhusudhan, N. 2017, ArXiv e-prints
Mandel, K., & Agol, E. 2002, ApJ, 580, L171
Marley, M. S., Gelino, C., Stephens, D., Lunine, J. I., & Freedman, R. 1999, ApJ, 513, 879
Marley, M. S., Saumon, D., Guillot, T., et al. 1996, Science, 272, 1919
Marley, M. S., Seager, S., Saumon, D., et al. 2002, ApJ, 568, 335
McCullough, P., & MacKenty, J. 2012, Considerations for using Spatial Scans with WFC3, Tech. rep.
McKay, C. P., Pollack, J. B., & Courtin, R. 1989, Icarus, 80, 23
Mordasini, C., van Boekel, R., Mollière, P., Henning, T., & Benneke, B. 2016, ApJ, 832, 41
Morley, C. V., Fortney, J. J., Marley, M. S., et al. 2015, ApJ, 815, 110
Morley, C. V., Knutson, H., Line, M., et al. 2017, AJ, 153, 86
Moses, J. I., Madhusudhan, N., Visscher, C., & Freedman, R. S. 2013, ApJ, 763, 25

Moses, J. I., Visscher, C., Fortney, J. J., et al. 2011, ApJ, 737, 15
Parmentier, V., Fortney, J. J., Showman, A. P., Morley, C., & Marley, M. S. 2016, ApJ, 828, 22
Rothman, L. S., Gordon, I. E., Barbe, A., et al. 2009, J. Quant. Spec. Radiat. Transf., 110, 533
Rothman, L. S., Gordon, I. E., Barber, R. J., et al. 2010, J. Quant. Spec. Radiat. Transf., 111, 2139
Rothman, L. S., Gordon, I. E., Babikov, Y., et al. 2013, J. Quant. Spec. Radiat. Transf., 130, 4
Saumon, D., & Marley, M. S. 2008, ApJ, 689, 1327
Sharp, C. M., & Burrows, A. 2007, ApJS, 168, 140
Showman, A. P., Fortney, J. J., Lian, Y., et al. 2009, ApJ, 699, 564
Sing, D. K., Fortney, J. J., Nikolov, N., et al. 2016, Nature, 529, 59
Stevenson, K. B. 2016, ApJ, 817, L16
Stevenson, K. B., Désert, J.-M., Line, M. R., et al. 2014, Science, 346, 838
Stevenson, K. B., Lewis, N. K., Bean, J. L., et al. 2016, PASP, 128, 094401
Swain, M. R., Line, M. R., & Deroo, P. 2014, ApJ, 784, 133
Tennyson, J., & Yurchenko, S. N. 2012, MNRAS, 425, 21
Tinetti, G., Tennyson, J., Griffith, C. A., & Waldmann, I. 2012, Philosophical Transactions of the Royal Society of London Series A, 370, 2749
Toon, O. B., & Ackerman, T. P. 1981, Appl. Opt., 20, 3657
Venot, O., Hébrard, E., Agúndez, M., et al. 2012, A&A, 546, A43
Wakeford, H. R., Sing, D. K., Evans, T., Deming, D., & Mandell, A. 2016, ApJ, 819, 10
Wakeford, H. R., Stevenson, K. B., Lewis, N. K., et al. 2017, ApJ, 835, L12
Waldmann, I. P. 2016, ApJ, 820, 107
Waldmann, I. P., Rocchetto, M., Tinetti, G., et al. 2015a, ApJ, 813, 13
Waldmann, I. P., Tinetti, G., Rocchetto, M., et al. 2015b, ApJ, 802, 107

APPENDIX

Here we present the retrieval results as described in Section 3. We present the pairs plots and fit to the observations in each case. In the case of the Line and Waldmann results we show both the thermochemically-consistent run along with the free retrieval for comparison.

BLECIC & CUBILLOS

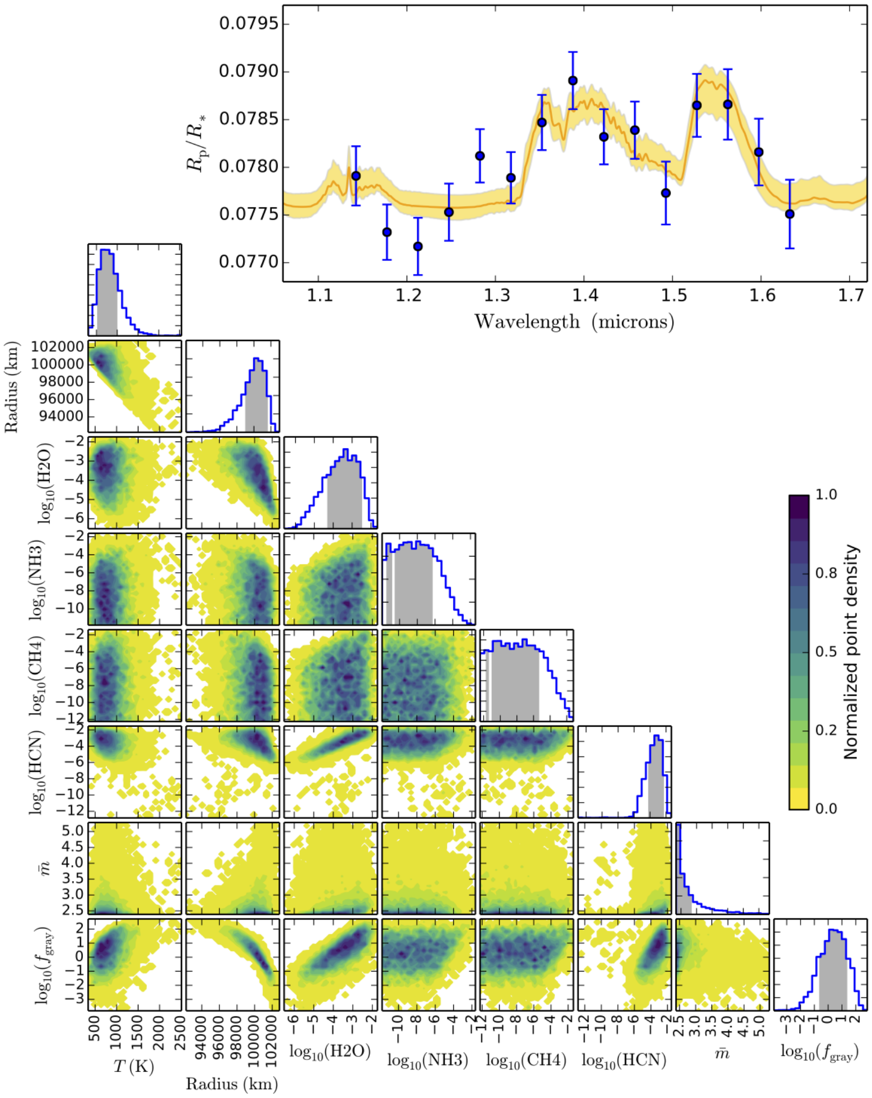

FIG. 6.— Posteriors and fit from retrieval parameterized by free abundances of H_2O, NH_3, CH_4, and HCN along with the mean molecular mass of the atmosphere. The atmosphere is assumed to be isothermal (T as a free parameter) with a grey cloud (opacity as free parameter).

LINE

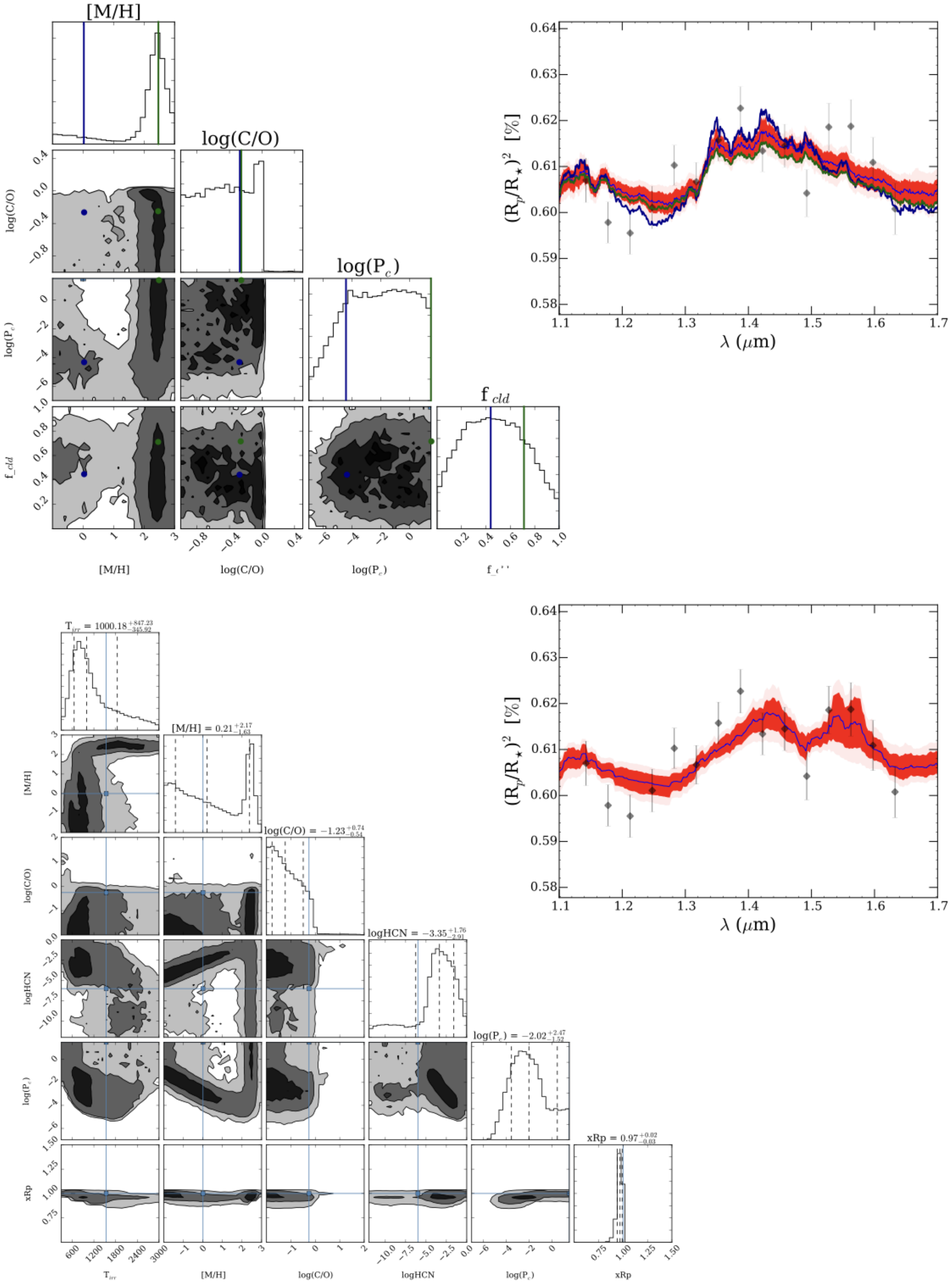

FIG. 7.— *Top:* Posteriors and fit to spectrum of thermo-chemically consistent retrieval. The elemental abundances are parameterized by the metallicity [M/H], the carbon-to-oxygen ratio log(C/O), and the carbon- and nitrogen-species quench pressures. *Bottom:* Posteriors and fit to spectrum of assuming a thermo-chemically consistent atmosphere with the addition of HCN as a free parameter.

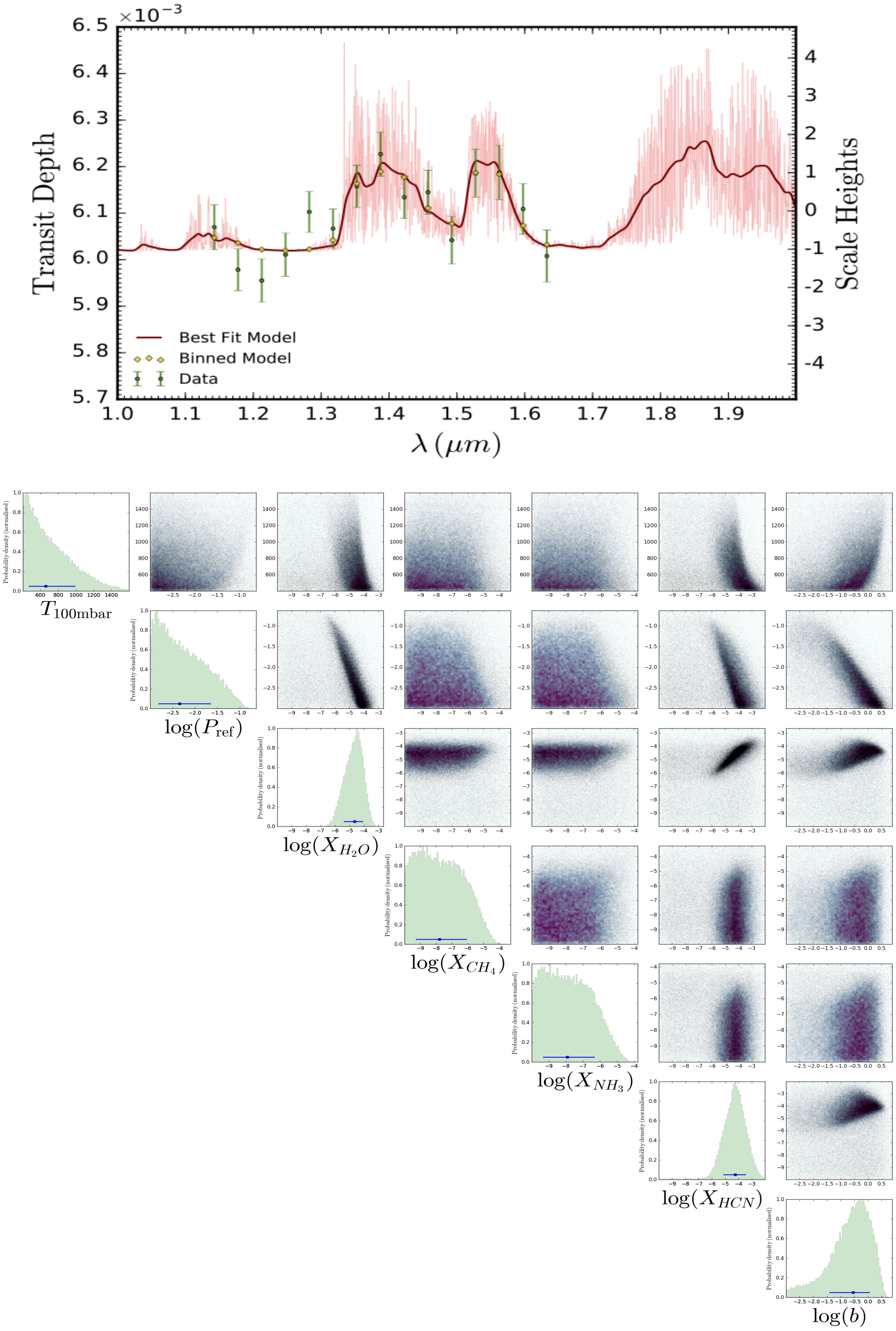

FIG. 8.— *Top:* Fit to spectrum of free retrieval. *Bottom:* Posteriors of free retrieval assuming an isothermal temperature-pressure profile, including molecular opacities due to H_2O, CH_4, NH_3, and HCN, and clouds as a uniform-in-altitude gray opacity.

WALDMANN

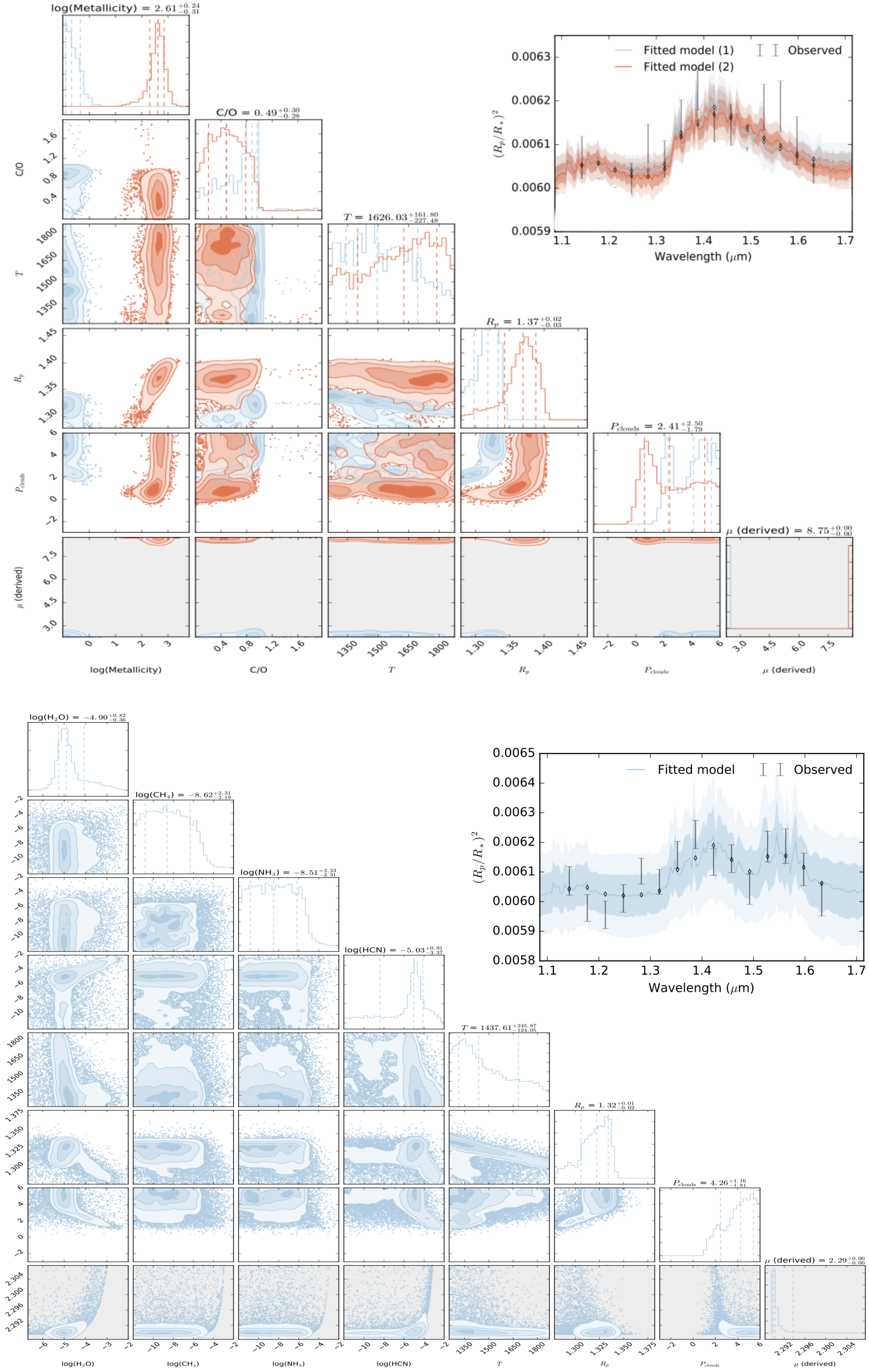

FIG. 9.— *Top:* Posteriors and fit to spectrum of chemically consistent retrieval. The free parameters are the C/O ratio, atmospheric metallicity, planet radius, temperature and cloud-top pressure. *Bottom:* Posteriors and fit to spectrum of free retrieval with planet radius, temperature, cloud-top pressure and abundances of H_2O, CH_4, CO, CO_2, NH_3, and HCN as free parameters.